CRYSTALLOGRAPHIC SOFTWARE

Parametric Study of Microstructural Properties at Laser Cladding

M. D. Khomenko[a,*], F. Kh. Mirzade[a], and V. G. Niziev[a]

[a] *Institute on Laser and Information Technologies, Federal Scientific Research Center "Crystallography and Photonics"*
(Shatura Branch), Russian Academy of Sciences, Shatura, Moscow oblast, 140700 Russia
***e-mail: hmd@laser.ru**
Received June 20, 2017; revised June 20, 2017; accepted June 20, 2017

Abstract—Self-consistent numerical model of laser cladding with coaxial powder injection has been developed. The model takes into account the heat transfer, hydrodynamics, solute transport, and phase transition kinetics. The additive process is numerically analyzed using the open-source computational fluid dynamics (CFD) package. The S-CLSVOF program is adapted for modeling heat and mass transfer and free boundary evolution of the melt pool. The phase transition is modeled using the Johnson−Mehl−Avrami−Kolmogorov equation with allowance for nonuniform temperature distribution on the melt pool surface. The clad-layer microstructure is investigated as a function of the process parameters. High scan rate is shown to result in a finer grain size of clad layer structure. The data obtained can be used for construct a cladding process map.

INTRODUCTION

Powders of heat-resistant alloys are widely used to repair parts of gas-turbine engines by laser gas-powder cladding [1, 2]. The microstructure of claddings is most often studied by analyzing experimental cuts [3, 4]; however, these methods are extremely complicated and expensive. Nondestructive fault detection methods are also used [5]. To search for the optimal regimes of formation of a defect-free material and products with a quality comparable to that of cast forms, one must gain a deep insight into the corresponding physical processes and phenomena. The development of physical and mathematical models based on numerical methods makes it possible to efficiently investigate and optimize laser cladding.

The multiscale approach (when the temperature history calculated on macroscale is used for microscopic calculations) is widely used to simulating microstructure at laser cladding [6, 7]. Another popular approach is the phase-field method, which is applied to describe the shape and sizes of the grains formed. However, this method is rather complicated, whereas it is often sufficient to know the average grain size of the product for real qualitative estimation of microstructure; therefore, simpler models can be used.

In this paper, we report the results of parametric study of laser cladding of powders of heat-resistant alloys in order to develop a microstructural map of the process. This map, which can be applied in wide ranges of various parameters, is efficient for finding the optimal treatment regimes. The microstructure was calculated using the adapted Johnson−Mehl−Avrami−Kolmogorov equation [8], the solution to which is in agreement with the equations of hydrodynamic heat transfer and clad bead free surface.

BASIC EQUATIONS

The macromodel is based on the model proposed in [9]. The main driving forces are surface thermocapillary and capillary forces [10], which play the role of volume sources in the velocity equation [11]. The free metal−gas interface is traced using the method that was reported in [12] and verified in [13] for multiphase media with thermocapillary forces. The PISO algorithm [14] is used to provide pressure−velocity coupling. The melting is assumed to be isothermal and the hydrodynamics in the transition regions is simulated by introducing a porous layer [15]. Powder is assumed to be captured by only the melt pool. The system of equations for the developed self-consistent model of laser cladding can be written as follows.

Continuity equation:

$$\frac{\partial \rho}{\partial t} + \nabla(\rho u) = 0. \tag{1}$$

Heat-transfer equation:

$$c\rho \frac{\partial T}{\partial t} + \nabla(c\rho u T) = \text{div}(\lambda \nabla T) + \alpha_{\text{beam}} q \delta(\varphi)$$
$$+ \rho(1 - f_l)\Delta c \frac{\partial T}{\partial t} - \rho L \frac{\partial f_l}{\partial t}. \tag{2}$$

Momentum equation:

$$\frac{\partial \rho u_i}{\partial t} + \nabla(\rho u u_i) = \text{div}(\mu \nabla u_i)$$
$$- \frac{C_{\text{big}}(1 - f_l)^2}{f_l^3 + C_{\text{small}}} - \frac{\partial \rho}{\partial i} + \nabla T \frac{\partial \sigma}{\partial t} \mathbf{i}. \tag{3}$$

Free-surface equation:

$$\frac{\partial \alpha}{\partial t} + \nabla(u\alpha) = F_{\text{powder}} |\nabla \alpha|. \tag{4}$$
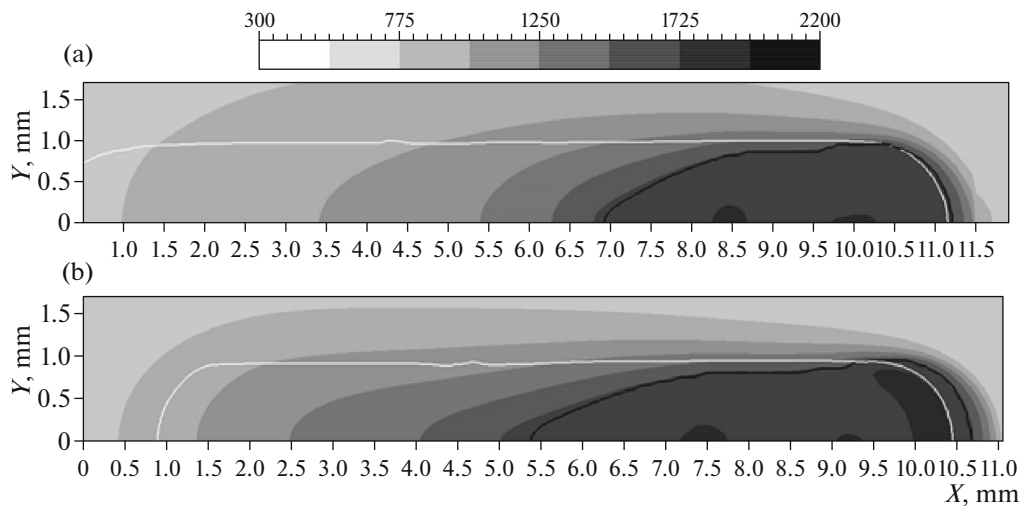
Fig. 1. Longitudinal cross-section of the clad bead at the substrate level for (a) low- and (b) high-speed sets of process parameters.

Here, t is time; p is pressure; T is temperature; c is the specific heat; ρ is the density; λ is the thermal conductivity; f_l is the liquid-phase volume fraction; u_i is the liquid-velocity component along the corresponding axis ($i = x, y, z$); μ is the viscosity; α is the VOF (Volume of Fluid) function for a free surface; F_{powder} is the free-surface velocity due to powder addition; and C_{big} and C_{small} are constants equal to 10^8 and 10^{-6}, respectively. The phase transition is simulated using the Johnson−Mehl−Avrami−Kolmogorov equation [16, 17].

$$f_l = 1 - \exp(f_l^{ext}), \qquad (5)$$

where f_l^{ext} is the volume fraction of the "extended" liquid phase. The details of this approach, which were reported in [18, 19], are omitted here.

We should dwell on the method for determining the initial crystallization conditions. If $J(T)$ is the local nucleation rate, which depends on time t in terms of temperature, the number of particles arising in the crystallization-zone volume V for this time is:

$$N = \int_t J(T)V dt. \qquad (6)$$

It is believed that crystallization is initiated when the number of nuclei reaches a specified value. A too large number of initial nuclei delays the crystallization onset and affects the average crystallite size. Too small N values lead to longer thermal history (and call for a higher memory space to store it); however, they do not affect the result. Therefore, one should find the optimal N value that does not affect the result and corresponds to not very long thermal history. In this study, we took the N value to be 1.

RESULTS AND DISCUSSION

High-quality laser cladding can be performed under various laser irradiation conditions. This process may have several windows of optimal parameters: at high and low scan rates. The laser power must be chosen proceeding from the scan rate. Figure 1 shows the melt pools for different scan rates and laser powers. Two sets of parameters were used: power $P = 400$ (640) W, absorption coefficient 0.45, beam radius $R = 1$ mm, powder feed rate $F = 4$ (10) g/min, trapping coefficient 0.9, powder-flow width $d = 2$ mm, and scan rate $V = 20$ (50) mm/s (the parameters for the high scan rate are given in parentheses). The laser radiation distribution in the beam was assumed to be uniform (unless otherwise specified) in the calculations. The parameters of materials were the same as in [18]. The average crystallite size is mainly affected by the activation energy E_a and phase interface energy γ. We used the following values: $E_a = 1.25$ eV and $\gamma = 70$ erg/cm^2.

Under conditions of high-speed cladding the melt-pool profile is elongated. A sharp temperature gradient arises at the laser-spot edges, whereas at the melt-pool periphery the temperature gradient ispractically zero. The sharp temperature gradient is due to the finite size of the laser source, and the weak variation in temperature is explained by the release of latent crystallization heat beyond the source. In the case of low scan rate, the temperature distribution in the melt pool is similar, but the melt pool is less elongated.

Figure 2 shows a typical pattern of hydrodynamic flows in the longitudinal and transverse cross-sections of the melt pool (the temperature gradient is indicated in shades of gray) in the case of Gaussian beam distribution. It can be seen that the hydrodynamic heat transfer determines the clad-bead geometry and, therefore, the crystallization-zone heat sink. An analysis of various laser beams (with Gaussian and uni-
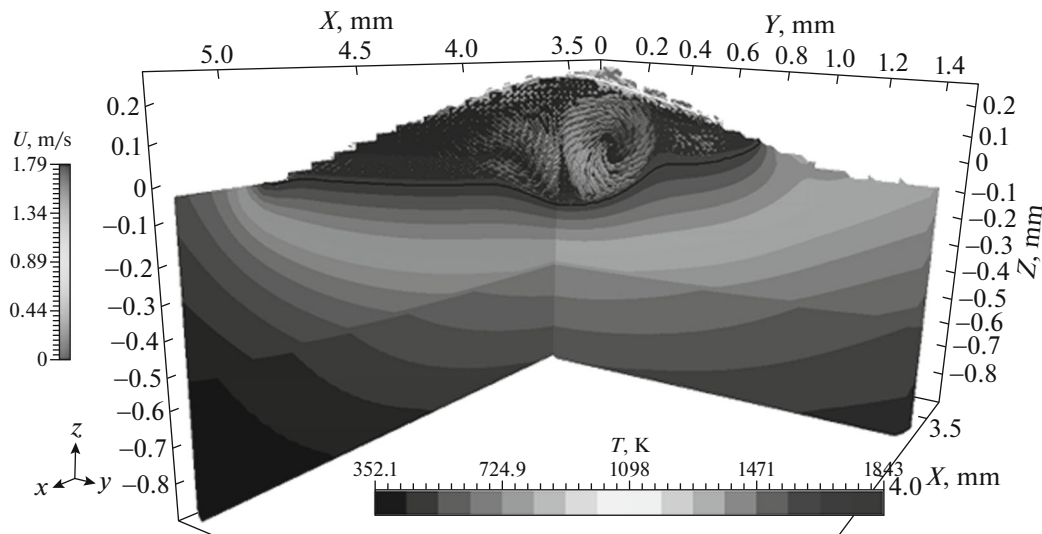
Fig. 2. Typical hydrodynamic flow in the transverse and longitudinal cross-sections of the melt pool.
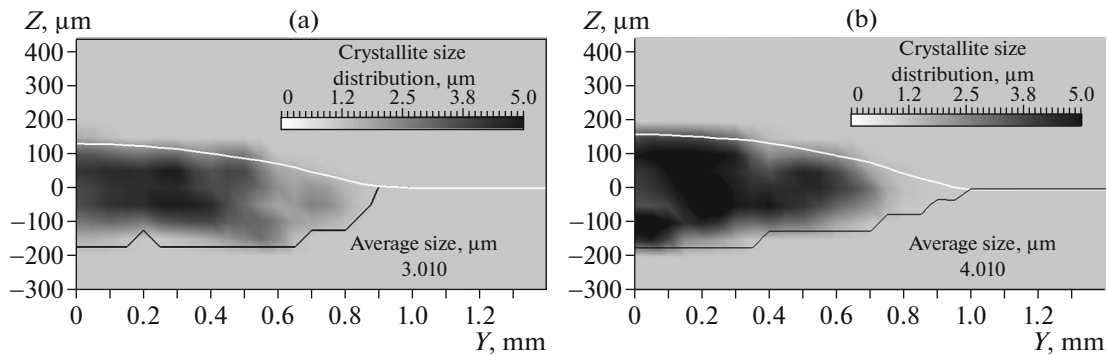

Fig. 3. Distribution of average crystallite sizes in the transverse cross-section of the clad bead.

form distributions) shows that the hydrodynamic heat-transfer intensity is determined by the radiation distribution. Primarily, this phenomenon is due to the fact that the thermocapillary forces, which depend on the temperature gradient, provide hydrodynamic motion in the melt pool. When a beam with a Gaussian distribution is used, the temperature gradients are somewhat weaker and shifted from the melt-pool periphery.

The distributions of the average crystallite radii in the clad-bead transverse cross section for the low- and high-speed sets of parameters are shown in Fig. 3. The clad-bead contour and level of metal substrate are indicated by bright curves and the recrystallization zones are shown by dark curves. The parameters are chosen so as to make the bead geometries similar at different scan rates. It can be seen that the average crystallite radius is larger in the case of slow cladding. Close scan rates barely affect the average crystallite size; however, a strong difference between the process

parameters leads to an evident difference in the clad-layer microstructures. Higher cooling rates result in a finer grain structure.

One needs only few reference experimental values of the average grain size at specified parameters to verify the results obtained. Thus, the process can be efficiently mapped from the point of view of obtaining a desired microstructure. Crystallization is initiated only after supercooling at a certain rate. Figure 4 shows the dynamics of changes in the temperature and volume fraction of the solid phase at a check point ($Y = 0.375$ mm, $Z = -0.025$ mm) for two sets of cladding parameters. One can observe a difference in the cooling rate in the initial stage, when the latent heat of crystallization is insignificant (Fig. 4a). In this stage, the higher scan rate corresponds to a cooling rate of about 15000 K/s, whereas the cooling rate for the low-speed set of parameters is smaller by a factor of three: ~5000 K/s. When the necessary supercooling is achieved, intense formation and growth of crystalline-
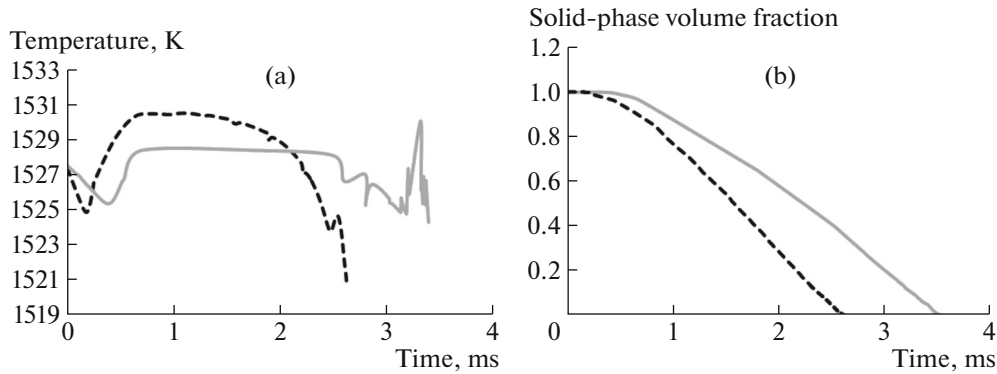
Fig. 4. Dynamics of the (a) temperature and (b) new-phase volume fraction at the check point for (solid lines) low- and (dashed lines) high-speed sets of parameters.

phase nuclei begin. At high and lower cooling rates, the maximum supercooling in the initial stage is 8.2 and 7.7 K, respectively. Then the supercooling is eliminated due to the release of latent heat of crystallization. At more intense supercooling, a larger number of crystallites is formed, whose rapid growth reduces supercooling to a greater extent (to 2 K). At a low cooling rate, the supercooling is reduced to a lesser extent (to ~4 K). This difference in the temperature dynamics leads to a difference in the dynamics of the crystallized-phase volume fraction (Fig. 4b) and, as a consequence, to new microstructural characteristics and stresses in the clad bead.

CONCLUSIONS

The distribution dynamics of the temperature, concentration, and phase fields in the melt pool and the free-surface motion under hydrodynamic forces and with powder added were calculated. The hydrodynamic heat transfer depends on the laser radiation distribution in the beam cross section. It determines the clad-bead geometry and, therefore, the crystallization-zone heat sink. The large difference in the process parameters leads to a large difference in the clad-layer microstructures. Higher cooling rates lead to finer grain structures. The results obtained make it possible to develop practical recommendations on the realization of optimal regimes of processing and monitoring the clad-material structure.

FUNDING

REFERENCES

1. A. G. Evgenov, S. I. Shcherbakov, and A. M. Rogalev, Aviatsionnye Mater. Tekhnol. **S1** (43), 16 (2016).
2. E. N. Kablov, A. G. Evgenov, O. G. Ospennikova, et al., Izv. Vyssh. Uchebn. Zaved.,Mashinostr. **9** (678), 62 (2016).
3. Y. Tian, D. McAllister, H. Colijn, et al., Metall. Mater. Trans. A **45**, 4470 (2014).
4. A. G. Evgenov, E. A. Lukina, and V. A. Korolev, Nov. Materialoved. Nauka Tekh. **5** (23), 1 (2016).
5. N. P. Aleshin, V. V. Murashov, A. G. Evgenov, et al., Defektoskopiya, No. 1, 48 (2016).
6. Y. Cao and J. Choi, J. Laser Appl. **18** (3), 245 (2006).
7. P. Nie, O. A. Ojo, and Z. Li, Acta Mater. **77**, 85 (2014).
8. D. Crespo and T. Pradell, Phys. Rev. B **54** (5), 3101 (1996).
9. V. G. Niz'ev, M. D. Khomenko, and F. Kh. Mirzade, Kvantovaya Elektron. **48** (8), 743 (2018).
10. X. He and J. Mazumder, J. Appl. Phys. **101**, 053113 (2007).
11. K. Yokoi, J. Comput. Phys. **278**, 221 (2014).
12. A. Albadawi, D. B. Donoghue, A. J. Robinson, et al., Int. J. Multiphase Flow. **53**, 11 (2013).
13. T. Yamamoto, Y. Okano, and S. Dost, Int. J. Numer. Meth. Fluids. **83**, 223 (2017). https://doi.org/10.1002/fld.4267
14. F. Moukalled, L. Mangani, and M. Darwish, *The Finite Volume Method in Computational Fluid Dynamics: An Advanced Introduction with OpenFOAM and Matlab* (Springer, London, 2016).
15. V. R. Voller and C. Prakash, Int. J. Heat Mass Transfer. **30** (8), 1709 (1987).
16. J. W. Christian, *The Theory of Transformations in Metals and Alloys* (Elsevier Science, Oxford, 2002).
17. V. Z. Belen'kii, *Geometric Probabilistic Models of Crystallization* (Nauka, Moscow, 1980) [in Russian].
18. F. K. Mirzade, M. D. Khomenko, and V. G. Niziev, Opt. Quantum Electron. **48**, 513 (2016).
19. M. D. Khomenko, V. Y. Panchenko, V. G. Niziev, et al., Bull. Russ. Acad. Sci.: Phys. **80** (4), 381 (2016).

Translated by Yu. Sin'kov